Journal of Materials Chemistry C

ROYAL SOCIETY OF CHEMISTRY

PAPER

View Article Online
View Journal

Cite this: DOI: 10.1039/d5tc04437e

Evaluation of Mn^{2+} sulfonylcalixarene complex-based materials for oxygen sensing

L. Bois, *[a] L. Mailler,[a] T. Grange,[a] G. Ledoux,[b] E. Jeanneau[a] and C. Desroches[a]

Complexes based on Mn^{2+} ions and the sulfonylcalixarene ($ThiaSO_2$) macrocycle are being studied as oxygen sensors. The anionic complex $[Mn_4(ThiaSO_2)_2F]^-$ exhibits oxygen-sensitive photoluminescent properties. Two counter anions, potassium (K^+) or tetrabutylammonium (TBA^+) cations, are used to obtain large crystals consisting of assemblies of anionic tetranuclear complexes, using a solvothermal process. A method for obtaining small particles from large crystals is proposed, based on dissolution in dimethylformamide and reprecipitation. This transformation of crystals into particles leads to a structural and textural reorganization that greatly enhances oxygen reactivity. Photoluminescence measurements are performed under controlled oxygen concentration and very good sensitivity to oxygen is observed in both particles, which highlights the enormous impact of structure and texture on luminescent properties. Particles assembled with potassium cations are highly sensitive to oxygen between 0 and 10%. Particles assembled with TBA cations have lower oxygen sensitivity but are more consistent in the 0–20% range, which proves that structural effects finely modulate the oxygen sensitivity. Particle shaping tests are carried out in two polymer matrices, polystyrene (PS) and polyisobutyl methacrylate (PIBMA), which show that the supported particles have retained their properties and that the oxygen response dynamics are very fast. These complexes, which are much more economical than noble metal complexes, are therefore very promising candidates for oxygen detection.

Received 19th December 2025,
Accepted 13th February 2026

DOI: 10.1039/d5tc04437e

rsc.li/materials-c

Introduction

Oxygen is essential for respiration and provides the energy needed for many physiological processes.[1] Detecting oxygen content is important in many fields, such as analytical chemistry, environmental monitoring and medical diagnostics.[2–6] Highly accurate, rapid and non-invasive monitoring of oxygen levels is an important requirement. Traditional oxygen monitoring processes, such as amperometry, conductimetry, and magnetic resonance techniques, have certain disadvantages: continuous measurements are difficult and response times are limited.[7–9] Sensor robustness and maintenance also pose problems. In contrast, the optical method is sensitive, non-invasive and fast. One way to measure this is to use photoluminescence measurements, as certain polycyclic aromatic compounds[10–12] and metal complexes[13–17] exhibit oxygen-sensitive photoluminescence properties. The process is based on the collision between molecular oxygen and the excited electronic state of the complex, and involves a decrease in intensity and decay time.[1] The relationship between the luminescence signal and oxygen concentration is described using the Stern–Volmer equation, which establishes a linear dependence in the simplest case. This predictable behaviour forms the basis for the operation of luminescent oxygen sensors and enables accurate quantification of oxygen. Long decay times are well suited as quenchability increases with them. Well-known metal–ligand complexes include polypyridyl Ru(II), Ir(III) complexes, and Pd and Pt porphyrins, which are typically incorporated into polymer or sol–gel matrixes.[1,2,18–31] In order to avoid the use of these scarce and expensive compounds, it would be advantageous to replace them with manganese(II) complexes.[32] Many purely inorganic materials containing Mn(II) ions exhibit known photoluminescence properties, due to a transition between the $^4T_1$ state and the $^6A_1$ ground state. Various Mn(II) complexes have been developed, and control of the Mn(II) ion environment allows fine modulation of the emission properties.[33–41] One such family of complexes uses macrocyclic ligands, sulfonylcalixarenes.[33,35,42–44] In this family, an interesting complex is a tetranuclear compound composed of four Mn(II) ions coordinated to two *p-tert*-butylsulfonylcalix[4]arene ($ThiaSO_2$) macrocycles, designated $K[Mn_4(ThiaSO_2)_2F]$, which exhibit an intense emission and a long lifetime (approximately 1 ms).[33–35,44]

[a] Laboratoire des Multimatériaux et Interfaces, UMR CNRS 5615, 6, rue Victor Grignard, Université Lyon1-CNRS, 69622 Villeurbanne Cedex, France. E-mail: laurence.bois@univ-lyon1.fr
[b] Institut Lumière Matière, UMR CNRS 5306, 10 Rue Ada Byron, Université Lyon1-CNRS, 69622 Villeurbanne Cedex, France

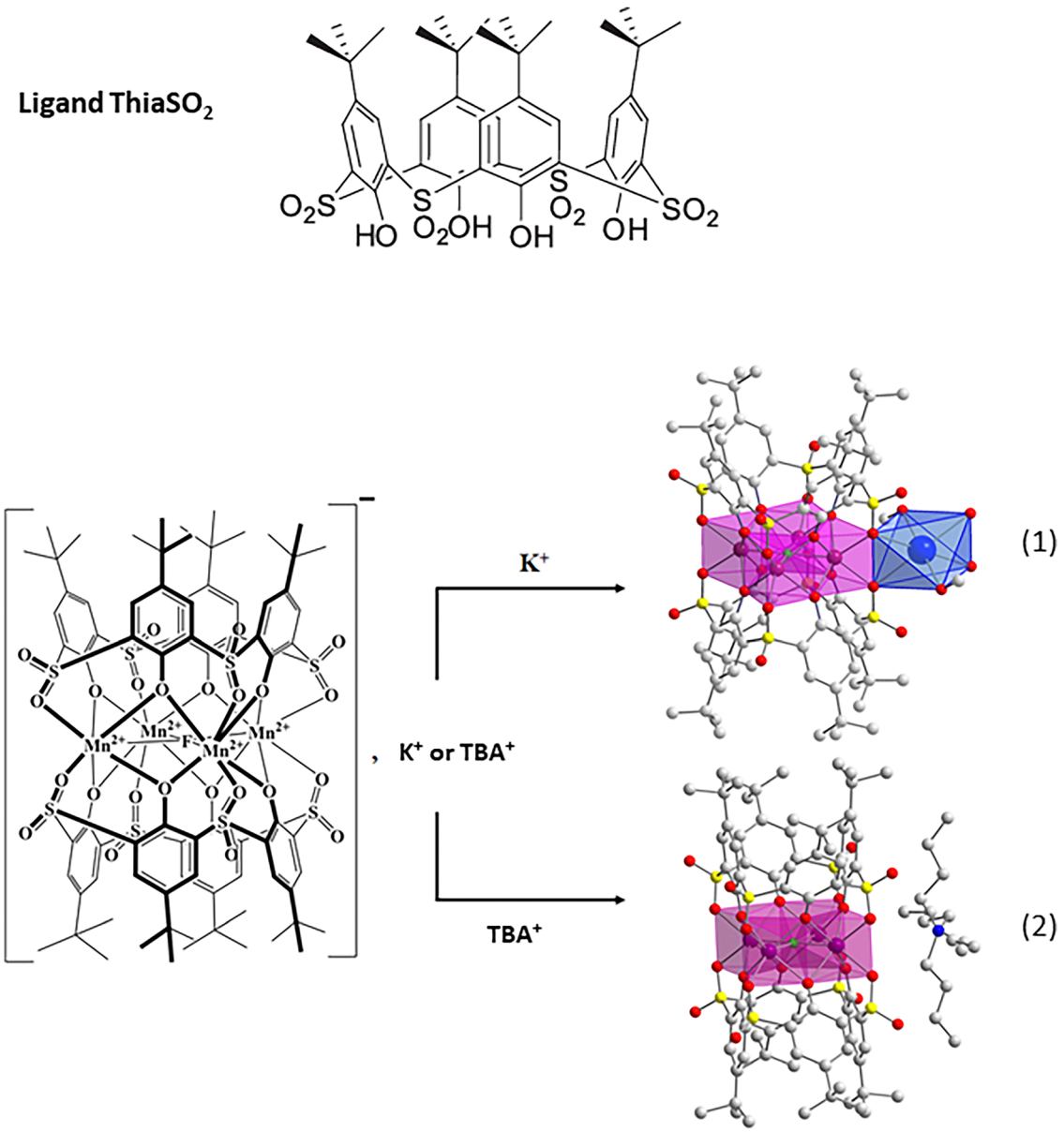

Fig. 1 View of the ligand $ThiaSO_2$, of the Mn-KF complex (**1**) and the Mn-TBAF complex (**2**) (F green, Mn purple, S yellow, O red, K blue, nitrogen blue, carbon grey).

In this tetranuclear system, the counter anion (K^+) is coordinated to the anionic complex $[Mn_4(ThiaSO_2)_2F]^-$ (Fig. 1). It is possible to form an assembly in which the coordinating potassium cation is replaced by a larger cation such as tetra-*n*-butylammonium (TBA^+), which is not coordinating. The resulting complex, $[TBA][Mn_4(ThiaSO_2)_2F]$ (**2**), exhibits photoluminescence that is highly sensitive to oxygen quenching.[43] In fact, lifetimes of 1.8 ms and 0.7 ms have been reported under vacuum and in air, respectively. For these complexes, the emission observed is that of Mn(II) ions and is caused by the 'antenna' effect of the sulfonylcalix[4]arene macrocycle. This ligand acts as a chromophore that absorbs UV excitation light and transfers energy from its T1 excited state to the $^4T_1$ excited state of Mn(II) ions.

In this work, we focused on developing oxygen-sensitive photoluminescent materials from these complexes. We studied Mn-KF-cryst (**1**) with a central fluoride and bridging potassium cations, as well as its cousin, the Mn-TBAF-cryst, with a central fluoride and TBA counter-cations (**2**). We then studied the transformation of large crystals of complex (**1**), whose solvothermal synthesis is best understood, into smaller particles (Mn-KF-part and Mn-TBAF-part) whose photoluminescence could be sensitive to oxygen. This transformation of complex (**1**) into particles Mn-KF-part was achieved by dissolution in the only solvent capable of dissolving this complex, dimethylformamide, followed by reprecipitation by introduction into an alcoholic solution. The influence of the presence of a cation (K^+ or TBA^+) at the time of precipitation was studied. The

photoluminescence properties of the particles obtained (Mn-KF-part or Mn-TBAF-part) are examined, and a material is then produced by dispersing the particles in a polymer support matrix based on polyisobutyl methacrylate (PIBMA) or polystyrene (PS) compositions.[2]

Experimental

Materials and methods

Mn-KF-cryst and Mn-TBAF-cryst synthesis. Commercial chemical reagents and solvents were used without further purification. The Mn-KF-cryst (**1**) and Mn-TBAF-cryst (**2**) crystals were prepared based on literature synthesis methods.[33,34,43,44] The synthesis of the ligand $ThiaSO_2$ is reported.[34] The alcoholic solution of the $MnCl_2$, $4H_2O$ salt was prepared by dissolving tetrahydrated $MnCl_2$, $4H_2O$ (25 mg, 0.126 mmol) (Alfa Aesar, Haverhill, MA, USA), in methanol (5 mL). Then, the ligand $ThiaSO_2$ (25 mg, 29.45 μmol) was added to the MeOH solution. After, a KF water solution (10 mg, 0.172 mmol, in 0.5 mL) was added to the solution. The mixture was heated for 2 days in a solvothermal bomb at 170 °C. After 48 h, the formed yellow crystals were separated from the solution and washed with a small amount of MeOH. In the synthesis of Mn-TBAF-cryst, the KF solution was replaced by a TBA fluoride solution.

Mn-KF-part and Mn-TBAF-part synthesis. To prepare the Mn-KF-part, the Mn-KF-cryst (**1**) (20 mg, 9.35 μmol) was dissolved in hot DMF (200 μL) and the solution was poured in an alcoholic solution (MeOH 3.5 mL and water 0.9 mL). A precipitation reaction is observed, and the particles were separated using centrifugation. To prepare Mn-TBA-part, the same protocol was used but some TBA fluoride salt (32 mg, 0.122 mmol) was added in the alcoholic solution.

Mn-KF-DMF-cryst (3) synthesis. To elucidate the structural differences between the starting Mn-KF-cryst (**1**) and the particle Mn-KF-part, the Mn-KF-cryst (**1**) (20 mg) was dissolved in hot DMF (200 μL) and crystal growth of Mn-KF-DMF-cryst (**3**) was carried out *via* vapor diffusion of methanol into the DMF solution of (**1**).

Particle-PIBMA or PS film preparation. To prepare the PIBMA film, the particles (Mn-KF-part or Mn-TBAF-part, resulting from 20 mg of the Mn-KF-cryst) were dispersed in a solution containing polyisobutylmethacrylate (M_w 20 000), PIBMA (125 mg) and THF (2.5 mL). Ultrasound was applied for 10 min before using a spin-coater to get a film on a glass substrate from this suspension. To prepare the PS film, the particles (resulting from 20 mg of the Mn-KF-cryst) were dispersed in a solution containing the polystyrene solution (800 μL), and xylene (2.5 mL). The polystyrene solution is obtained by dissolving at 60 °C for 4 hours, polystyrene (M_w 192 000, m = 6 g), tributylphosphate 97% (200 μL) in xylene (40 mL).[2]

Structural characterization

The crystal structure was defined by an X-ray powder diffractometer (Bruker D8 Advance diffractometer, Bruker, Billerica, MA, USA), equipped with the Cu Kα radiation (λ = 1.54060 Å). Powder XRD diagrams were collected under 45 kV and 30 mA at room temperature. EDS spectra were acquired on a Thermo Scientific Phenom Pharos G2 Desktop FEG-SEM. Scanning electron microscopy (SEM) images of the complexes and particles were captured using a Zeiss Merlin Compact (Zeiss, Germany) operating at 20 kV (Centre Technologique des Microstructures de l'Université de Lyon). Transmission electron microscopy (TEM) was performed on a JEOL 2100F field emission instrument operating at 200 kV (Centre Technologique des Microstructures de l'Université de Lyon). Textural characterization studies were done using nitrogen adsorption isotherms on a BelsorpMax (Bel Instruments, Japan). Prior to analysis, samples were outgassed under vacuum (100 °C for 12 h). The pore size distribution and the mesoporous volume were calculated from the adsorption branch of the isotherms using the Barrett–Joyner–Halenda (BJH) method between P/P_0 = 0.42 and 0.96. The total porous volume was measured at P/P_0 = 0.98 and the surface area were determined by the Brunauer–Emmett–Teller (BET) approach. The microporous volume was calculated using the *t*-plot method. Non-local density functional theory (NLDFT) pore size distribution was calculated using a cylinder model.

Optical characterization

The photoluminescent properties were analyzed using a homemade spectrofluorometer, equipped with a pulsed tunable OPO laser (EKSPLA NT230, 50 Hz). The laser spot was non-focused to protect the sample from being destroyed under high-power light. The emission light was collected by two optical fibers coupled to, on one side a Kymera328i spectrograph equipped with a cooled EMCCD detector (NewtonEM 970) for spectral measurement and on the other side to a Jobin Yvon TRIAX320 monochromator equipped with a cooled photomultiplier whose signal is fed to an MCS8A multichannel counter from FastComtec for the lifetime measurements ensuring a time resolution of 800 ps. The samples are placed inside a Linkam THMS600-PS stage in which a flow of gas is introduced. The gas composition can be controlled thanks to two SFC6000D-5slm mass flow controllers from Sensirion. The mass flow controllers are connected respectively to a nitrogen gas cylinder and a dry air gas cylinder. By changing the flow the atmosphere around the sample can be varied continuously from a pure nitrogen atmosphere to an atmosphere containing 20% oxygen.

For the S1 and S2 movies the sample is illuminated using a collimated 365 nm LED (M365L2-C2 from Thorlabs) working at 25 mW. The sample is imaged using a JAI GO 2400m camera equipped with a Zoom 7000-2 Macro Lens from Navitar and working in full frame at 98 fps. For the first movie (Movie S1), the sample is placed inside the chamber of the linkam stage with a flow of nitrogen, and at the beginning of the movie nitrogen is replaced by air and one can see the time the flow needs to establish. In the S2 movie the sample is under air and a 2 L min^{-1} flow of N_2 getting out of a 4 mm diameter tubing is brought close to the sample and moved around.

Results and discussion

Synthesis of the crystals and particles

The precursor crystals (**1**) and (**2**) were synthesized *via* a solvothermal method in methanol at 170 °C, using the $ThiaSO_2$ macrocycle, $MnCl_2{\cdot}4H_2O$ as the manganese source, and a fluoride salt—KF for Mn-KF-cryst (**1**) and TBAF for Mn-TBAF-cryst (**2**), according to procedures previously reported in the literature (Fig. 1). In both cases, the synthesis yielded a powder composed of single crystals several tens of micrometers in size, regardless of the dilution of the reaction mixture or the reaction time. To obtain a more dispersible powder composed of smaller particles in the submicrometer range, a rapid precipitation method was employed. The complexes were first dissolved in hot dimethylformamide (DMF) and then rapidly precipitated into a methanol/water mixture. This simple approach enables the formation of finer particles that are readily dispersible in alcoholic media. Particles of cryst (**2**) can also be obtained from Mn-KF-cryst (**1**) dissolved in DMF, followed by precipitation in a 1 M TBAF solution in a water/methanol mixture. The cation exchange between K^+ and TBA^+ follows the HSAB (hard and soft acids and bases) principle, considering that the anion $[Mn_4(ThiaSO_2)_2F]^-$ exhibits a soft character. Crystals (**1**) and (**2**) show low solubility, which justifies the use of polar solvents such as DMF. It has previously been reported that the anion $[Mn_4(ThiaSO_2)_2F]^-$, when dissolved in DMF, can transform into a neutral dinuclear complex of formula $(ThiaSO_2)Mn_2(DMF)_4(H_2O)_2$. However, for the particles $K[Mn_4(ThiaSO_2)_2F]$ and $TBA[Mn_4(ThiaSO_2)_2F]$ obtained using this procedure, mass spectrometry analyses confirm that no such transformation has taken place. The $[Mn_4(ThiaSO_2)_2F]^-$ anion remains intact throughout the dissolution and re-precipitation process, indicating the structural stability of the manganese tetranuclear complex under the experimental conditions employed.

Structural analysis of the crystals and particles

The X-ray diffraction pattern of Mn-KF-cryst, which shows a very intense reflection at 5.7° and additional peaks at 7.8°, 8.4°, and 8.9°, shows some similarities with the diagram calculated from single-crystal data (CCDC 824786), shown in Fig. 2a and Table S1.[34] However, the peaks appear to be shifted to slightly higher angles (by approximately 0.4°). The experimental diffraction pattern of the Mn-TBAF-cryst shows a main reflection at 5.1°, followed by weaker reflections at 8.2°, 8.7°, and 10.6°. Similar features can be observed in the calculated diagram (Fig. 2b and Table S1), although the main reflection in the calculated data is shifted to lower angles (4.9°, CCDC 2034491).[43] We hypothesize that the differences between the experimental and calculated diffraction patterns for the two crystals arise from the fact that the calculated patterns are based on single-crystal measurements performed at low temperature (100 K), without solvent loss, whereas the powder diffraction patterns were recorded at room temperature under ambient conditions. This behavior is common for this type of

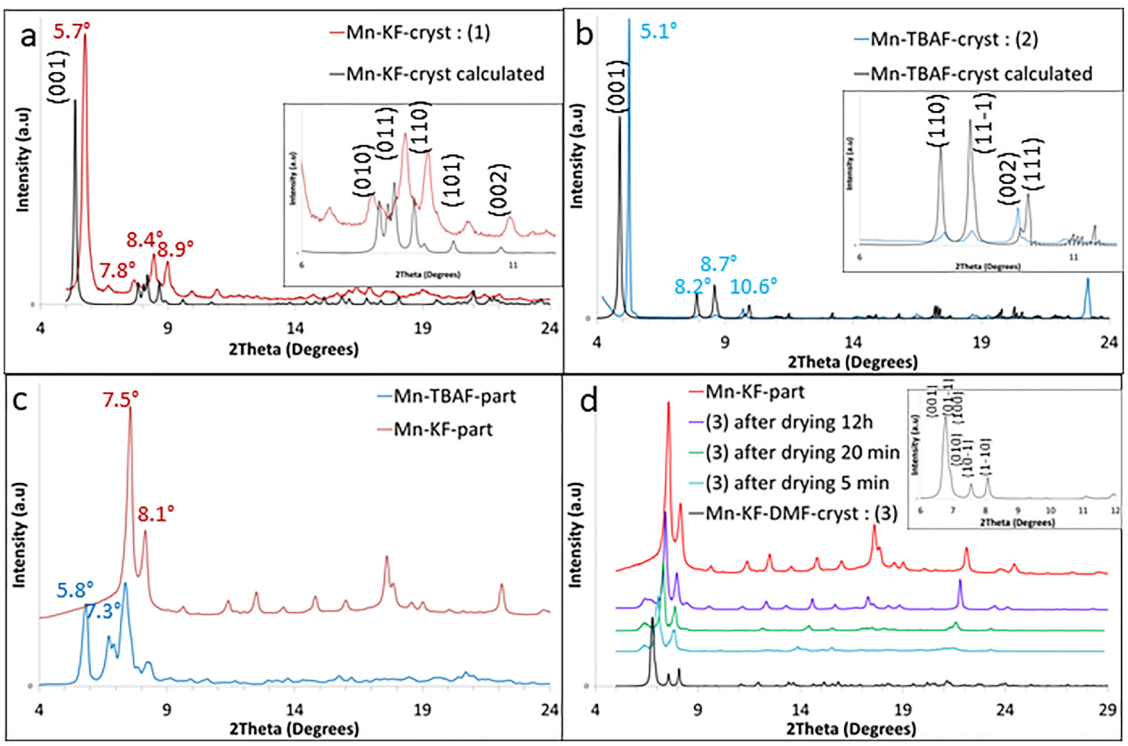

Fig. 2 X-ray diffraction patterns of the Mn-KF-cryst (a) and Mn-TBAF-cryst (b) (compared to the calculated pattern from monocrystal determination) and (c) the Mn-KF-part and MnTBAF-part. X-ray diffraction patterns the Mn-KF-DMF-cryst (**3**) dried at different steps (5 minutes, 20 minutes and 12 hours) and Mn-KF-part (d).

compound, which is capable of trapping solvent molecules. Nevertheless, it can be concluded that for both crystals, the overall crystal structures remain essentially identical, with only a slight contraction of the unit cell. The X-ray diffraction pattern of Mn-KF-part shows a doublet at 7.5° and 8.1° (Fig. 2c), while that of Mn-TBAF-part shows three main reflections at 5.8°, 6.7°, and 7.3° (Fig. 2c). These patterns differ significantly from those of the starting compounds, indicating a structural change that occurred during particle formation. One essential change in these powder diagrams is the disappearance of the very intense (001) line at low angles, which reflects a change of organisation of the chains between them. Nonetheless, for all syntheses performed, the diffraction patterns of the obtained particles exhibit similar profiles, indicating that these particles consist of a single and identical crystalline phase. Scanning electron microscopy (SEM) images reveal submicrometric particles in both cases (Fig. 3). Transmission electron microscopy images confirm that the Mn-KF-part are in the form of platelets approximately 150 nm long, 75 nm wide and 15 nm thick (Fig. S1). Energy-dispersive X-ray spectroscopy (EDS) confirmed the presence of potassium cations in Mn-KF-cryst and Mn-KF-part, while a nitrogen signal, attributed to the TBA^+ cation, was detected in Mn-TBAF-cryst and Mn-TBAF-part (Fig. S2). Mass spectrometry performed on both types of particles confirms the conservation of the $[Mn_4(ThiaSO_2)_2F]^-$ anion (Fig. S3). Infrared spectroscopy (FTIR) also confirms the conservation of the vibrational profile between the initial crystals and the particles. However, it reveals the presence of residual DMF molecules in the particles, as evidenced by the appearance of a new band at 1660 cm^{-1} (Fig. S4).[33,45] This observation suggests that one of the changes between the initial crystals and the particles is related to the presence of DMF molecules. Nitrogen adsorption isotherms of Mn-KF-cryst and Mn-KF-part are of type I. Mn-KF-cryst has a specific surface area of 65 $m^2\ g^{-1}$ and a porous volume of 0.08 $cm^3\ g^{-1}$ (Fig. S5a and Table S2). It also shows that Mn-KF-part has a higher porosity compared to Mn-KF-cryst, with a specific surface area of 221 $m^2\ g^{-1}$ and a porous volume of 0.36 $cm^3\ g^{-1}$. A small microporous volume, from *t*-plot calculation, is noted in Mn-KF-cryst (0.01 $cm^3\ g^{-1}$), which is increased to 0.03 $cm^3\ g^{-1}$ in Mn-KF-part. The BJH pore size distribution shows small mesopores in Mn-KF-part (Fig. S5b). The NLDFT pore size distribution of MN-KF-cryst and Mn-KF-part shows a maximum around 1 nm (Fig. S5c). MnTBAF-cryst and Mn-TBAF-part are non-porous samples, with a specific surface area of 1 and 6 $m^2\ g^{-1}$, respectively. From XRD patterns, for both Mn-KF-part and Mn-TBAF-part, the precipitation-based preparation method leads to the formation of pseudo-polymorphs, in which the order of the (001) plane has been modified (Fig. 2c). Studies have shown that different stacking modes are observed for solvated crystal structures. This suggests that specific intermolecular interactions between calixarenes and certain solvents play a crucial role in the crystallisation process.[46–50] In the case of molecular crystalline compounds, polymorphism is a common phenomenon that can result from various factors such as temperature, crystallization solvent, or crystallization rate. To elucidate the structural differences between the starting crystals and the particles, several single-crystal growth attempts were carried out by vapor diffusion of methanol into DMF solutions of the crystals. For TBAF, the obtained crystals were of insufficient quality for single-crystal X-ray diffraction analysis. Conversely, for the Mn-KF-cryst, a crystal structure Mn-KF-DMF-cryst (**3**) could be determined (CCDC 2516881) (Table S1, Fig. S6). As in the initial Mn-KF-cryst structure, the Mn-KF-DMF-cryst (**3**) crystallizes as stacks of chains formed by alternating $[Mn_4(ThiaSO_2)_2F]^-$ anions and K^+ cations. However, in this case, the K^+ ions are coordinated only by one oxygen atom from the sulfonyl group of the macrocycle, with their coordination sphere completed by two DMF molecules and one methanol molecule (Fig. S6 and Table S1). This pseudo-polymorph also crystallizes in the $P\bar{1}$ space group.Fig. S7 shows surface contact with a probe of radius 1.2 Å (Mercury). The probe can be introduced inside the Mn-KF-DMF-cryst (**3**) structure 7. It could give one qualitative indication about the potential for oxygen diffusion (size 3 Å) within this structure. We must bear in mind that actual porosity may differ greatly from the porosity calculated from crystallographic data and therefore remain very cautious when establishing a relationship with oxygen diffusion. Indeed, one part of cavities is certainly at least partially occupied by DMF molecules. Nevertheless, the powder diffraction pattern of this pseudo-polymorph (**3**) does not match that obtained for the particles Mn-KF-part (Fig. 2d). By monitoring the evolution of the diffraction patterns of the Mn-KF-DMF-cryst (**3**) during solvent evaporation, we observe that the pattern of the Mn-KF-DMF-cryst (**3**) progressively approaches that of the Mn-KF-part (Fig. 2d). This behavior indicates a very close structural relationship between the two phases, with the differences in the diffraction patterns most likely arising from subtle structural changes associated with solvent loss. The weak interactions between the anion–cation chains favor multiple possible stacking arrangements, leading to the formation of different polymorphs. The transformation from the Mn-KF-cryst (**1**) into Mn-KF-DMF-cryst (**3**) led to an assembly of the same clusters which are now packed in a more flexible way, because the counter cation coordination is changing from 2 to 1 (Fig. S6). The structure of Mn-KF-part is the product of the drying of the Mn-KF-DMF-cryst (**3**).

Photoluminescent properties of particles

Mn-KF-cryst emits at 590 nm and the photoluminescence intensity shows moderate sensitivity to oxygen content when excited in the near UV (Fig. 4a). Mn-TBAF-cryst is highly photoluminescent and emit at 600 nm. In addition, luminescence is highly sensitive to oxygen (Fig. 4b). The properties of particles are different compared from those of crystals. Mn-KF part emit at around 593 nm and are highly sensitive to oxygen concentration (Fig. 4c). The intense luminescence observed under nitrogen is greatly attenuated at low oxygen concentrations. Luminescence intensity decreases by 28 between nitrogen and air. In contrast, Mn-TBAF-part emits at around 603 nm and also shows clear sensitivity to oxygen content (Fig. 4d). The

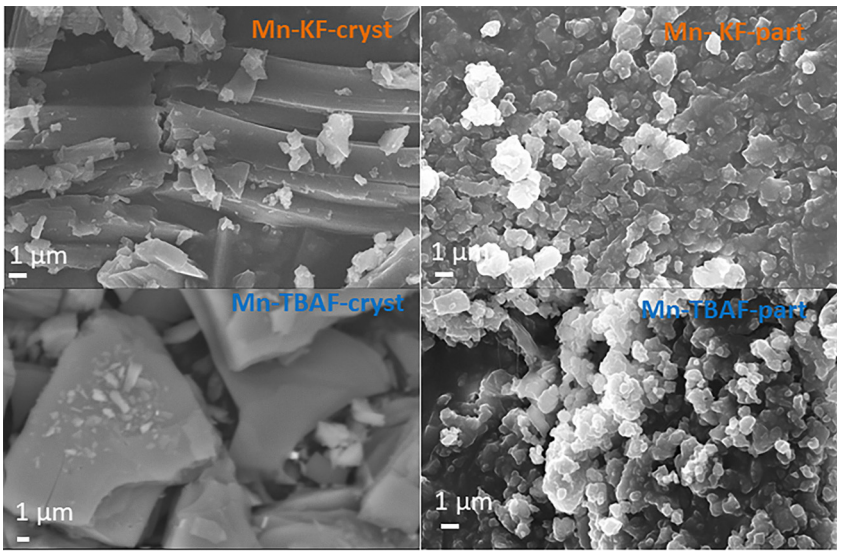

Fig. 3 SEM images of the MnThiaSO$_2$ KF and TBAF complexes and of the MnThiaSO$_2$ KF and TBAF particles.

decrease in intensity with increasing oxygen concentration is slower, but still considerable (factor 7). The Stern–Volmer equation is used to describe the ideal quenching system: $I_0/I = t_0/t = 1 + K_{sv}[O_2] = 1 + t_0 k_q[O_2]$ where K_{sv} is the Stern–Volmer constant, k_q the quenching constant, t_0 and I_0 decay and intensity in the absence of oxygen, respectively. Examination of the intensity curves relative to the intensity in the absence of oxygen I_0, I_0/I (Fig. S8), confirms that Mn-KF-cryst is almost insensitive to oxygen (K_{sv} = 0.017 kPa^{-1}). The Mn-TBAF-cryst is more sensitive than the Mn-KF-cryst (K_{sv} = 0.06 kPa^{-1}). In the case of particles, a very steep slope is observed, particularly for Mn-KF-part (K_{sv} = 0.27 kPa^{-1} for Mn-TBAF-part and K_{sv} = 1.32 kPa^{-1} for Mn-KF-part). It can also be seen that Stern's model is not very well suited for Mn-KF-part, as the curves are not linear, probably due to the presence of several populations.[19] Mn-KF part are highly sensitive to oxygen levels <15%. Mn-TBAF-part is less sensitive but more linear across the entire range of %O_2 observed. The observed deviation from linear Stern–Volmer behavior, noted in the case of Mn-KF-part, suggests the presence of multiple emissive populations subjected to different local oxygen environments, likely due to the particulate nature of the sensor and the presence of surface complexes directly exposed to oxygen and buried complexes incompletely affected by oxygen. It induces variations in the oxygen permeability within the particle. Such behavior is well-documented for oxygen-sensors and is commonly described using multi-site quenching models such as the Lehrer model. The data have been analyzed using a simplified Lehrer-type model assuming one oxygen-accessible emissive population and one effectively oxygen-inaccessible population. This assumption is supported by lifetime measurements, which are presented in the following paragraph, showing a long-lived component (t_{long}) that remains unchanged upon oxygen exposure (Fig. S9). In this more appropriate Lehrer representation, $I_0/\Delta I$ is represented as a function of $[O_2]^{-1}$ (Fig. 4, 2nd row, Table S3).[19] In this case, fraction f is quenchable while fraction $1 - f$ one is not. In Lehrer's representation, the ordinate at the origin $1/f$ reflects the importance of the proportion of quenchable sites (92% for Mn-KF-part and 99% for Mn-TBAF-part compared to 32% for the Mn-KF-cryst and 75% for the Mn-TBAF-cryst). The slope of the line is inversely proportional to the product of $K_{sv} \times f$. We can then estimate that the K_{sv} ratio is equal to 2.4 kPa^{-1} for Mn-KF-part and 0.5 kPa^{-1} for the Mn-TBAF-part. These values should be compared with those in the literature (Table S4), where K_{sv} values of approximately 3–4 kPa^{-1} are obtained for Pt-based compounds.[51] Highly sensitive compounds such as Pd porphyrins are known with K_{sv} reaching 68 kPa^{-1}.[1,52] Ruthenium polypyridyl compounds have K_{sv} about 1 kPa^{-1} and some Ir cyclometalated samples reach K_{sv} of about 27 kPa^{-1}.[25] The compounds in this work have K_{sv} between 0.5 and 2.4 kPa^{-1}, therefore exhibit luminescence with a considerable sensitivity to oxygen, comparable to Pt porphyrins or Ru polypyridyl compounds, even if the values are below that of Pd porphyrins, or Ir cyclometalated complexes. Certain organic compounds such as polyimides have a K_{sv} of 0.23 kPa^{-1},[12] while K_{sv} values of 13 kPa^{-1} have been observed in thianthrene based compounds.[11] The K_{sv} values are certainly lower than those of the most sensitive sensors, but nevertheless open up very interesting prospects, especially since the cost of these compounds is lower, by around 4 orders of magnitude, than that of compounds based on noble metals.

Lifetime measurements based on oxygen content were then performed (Fig. 5 and Fig. S9). The measurements confirm the low sensitivity of the Mn-KF-cryst (Fig. 5a). The high sensitivity to low oxygen contents is evident in the Mn-KF-part (Fig. 5c), where a very rapid decay is observed even at the lowest oxygen levels. The evolution of lifetimes is more regular in the case of TBAF compounds (Fig. 5b and d). The decline curves are bi-exponential. We therefore considered a first time zone t_{short}

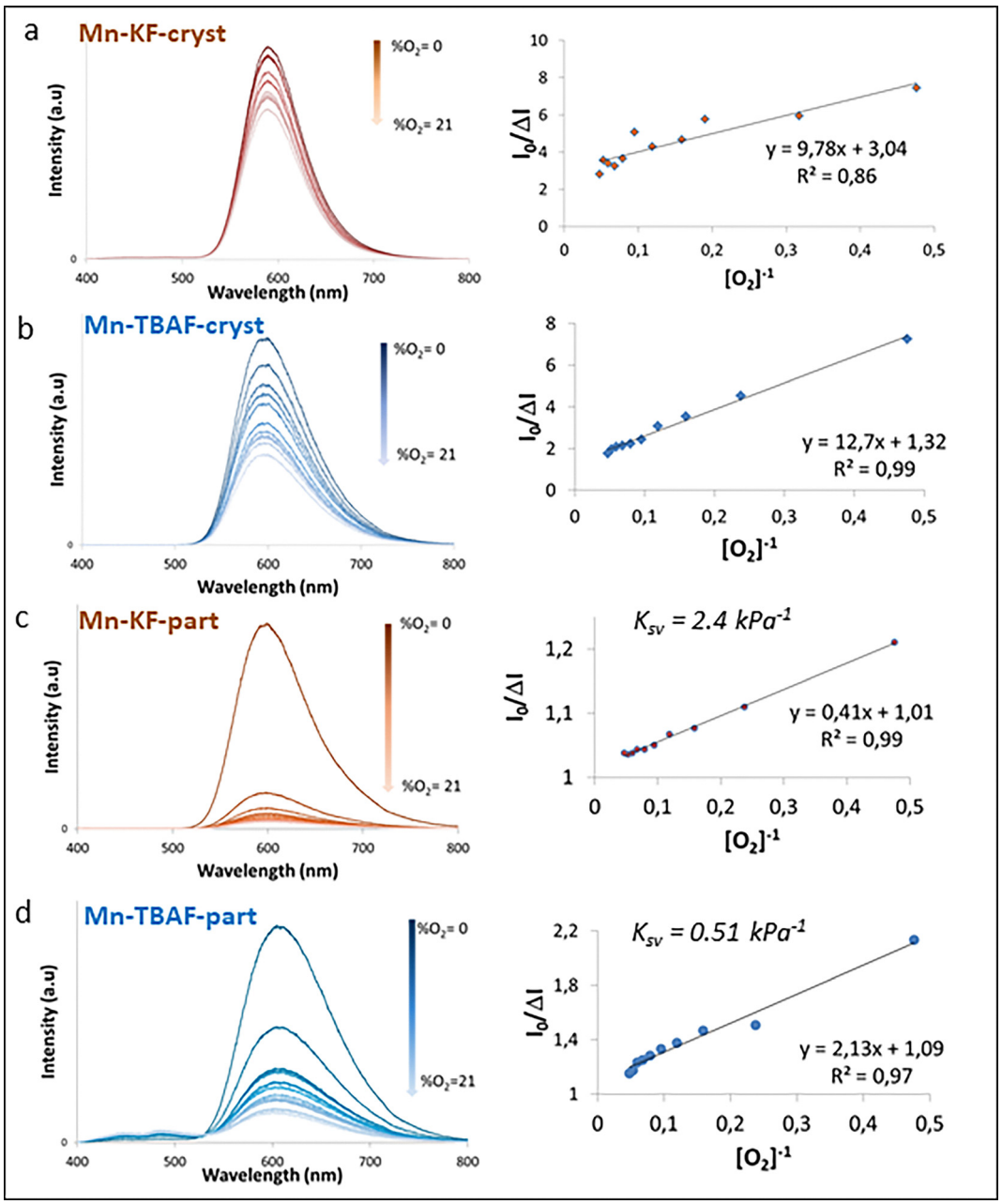

Fig. 4 Emission spectra of the Mn-KF-cryst (a) and Mn-TBAF-cryst (b) and of the Mn-KF-part (c) and Mn-TBAF-part (d) at different O_2%. $I_0/\Delta I$ curves *versus* $[O_2]^{-1}$ of the Mn-KF-cryst (a), Mn-TBAF-cryst (b) and of the Mn-KF-part (c), Mn-TBAF-part (d) at different O_2%.

between 0 and 150 μs and a second zone t_{long} for longer times between 0.6 and 2.6 ms. Examination of the slopes of the decay curves as a function of time in a time zone (t_{short} corresponding to the initial 150 μs) confirm the sensitivity of particles to oxygen (Fig. 5, 2nd row). The slope in the t_{short} range is very sensitive to % O_2 in the case of Mn-KF-part and Mn-TBAF-part and completely insensitive in the case of both crystals, suggesting that this is a surface phenomenon occurring over extremely short durations of approximately 200 μs. Very similar, bi-exponential decays have also been reported in the case of $[Ru(2,2\text{-bipyridine})_3]^{2+}$ confined inside a metal organic framework[53,54] or inside bock copolymers[55] which reinforces our belief that the rapid component t_{short} is explained by surface effects. The greater sensitivity of Mn-KF-part to lower oxygen concentrations is confirmed by examining the evolution of this decay time, which decreases very rapidly from 150 μs to 38 μs for an oxygen content increasing from 0% and 12%, then stabilizes. In contrast, for Mn-TBAF-part, the decrease in this time from 120 μs to 30 μs is more constant across the entire range of oxygen concentrations. Using the oxygen-sensitive lifetime component, Stern–Volmer analysis based on lifetimes yields a τ_0/τ ratio of approximately 4 at 21% O_2, corresponding to an apparent K_{sv} value of 0.14 kPa^{-1}. This confirms efficient oxygen quenching. Comparable τ_0/τ ratios are observed in the

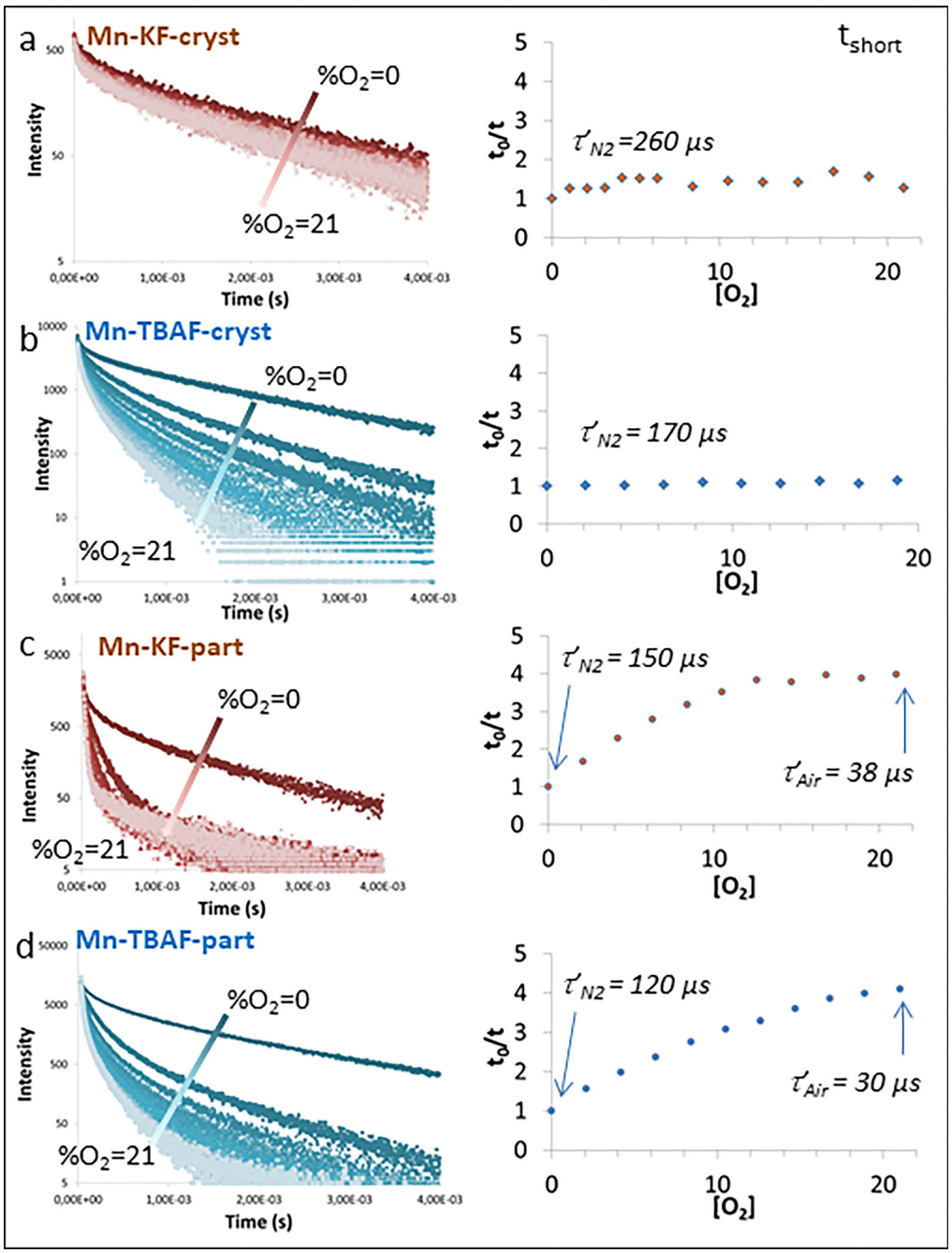

Fig. 5 Lifetime measurements of the Mn-KF-cryst (a) and Mn-TBAF-cryst (b) and of the Mn-KF-part (c) and Mn-TBAF-part (d) at different O_2%. Relative times of decay of the Mn-KF-cryst complex (a), Mn-KF-part (b) and Mn-TBAF-cryst (c), Mn-TBAF-part (d) at different O_2% in two temporal zones (t_{short} < 150 μs, t_{long} between 0.6 and 2.6 ms).

case of Ru and Ir compounds,[1,25] while Pd and Pt porphyrins present τ_0/τ ratio reaching 198 and 80, respectively (Table S4).[52] Examination of longer times (t_{long} between 0.6 and 2.6 ms) shows that the Mn-TBAF-cryst has a decay time that is very sensitive to oxygen content, and this time, of the order of 1.87 ms in the absence of oxygen, is consistent with the decay time of Mn^{2+} ions in the crystals observed previously (Fig. S9b).[35,43] The decay in Mn-KF-cryst, of 1.68 ms, is insensitive to oxygen content (Fig. S9a). In the case of Mn-KF-part (Fig. S9c), the slope in this time range, 1.31 ms, is not sensitive to oxygen content, whereas for Mn-TBAF-part (Fig. S9d), the decay time is 1.33 ms without oxygen and between 0.53 and 0.70 ms in the presence of oxygen. To resume, time-resolved photoluminescence measurements reveal a bi-exponential decay behavior for Mn-KF-part and Mn-TBA-part. Two distinct lifetime components are observed. A long-lived component of 1.3 ms is present under both N_2 and air atmospheres and remains essentially unchanged upon oxygen exposure (except

for Mn-TBAF-cryst). This component is therefore assigned to emissive sites that are poorly accessible to oxygen and do not contribute to oxygen sensing. In contrast, a shorter-lived component in the microsecond range (150 μs) exhibits a pronounced dependence on oxygen concentration. Under N_2, this oxygen-sensitive lifetime amounts to approximately 150 μs, while exposure to air reduces it to about 40 μs. This behavior is associated with the active sensing component. The simplified Lehrer model leads to a linear representation shown in Fig. S10, with a K_{sv} parameter of 0.42 and 0.32 kPa^{-1} for the Mn-KF-part and the Mn-TBAF-part, respectively. The coexistence of oxygen-sensitive and oxygen-insensitive emissive populations is consistent with heterogeneous oxygen accessibility in the solid state and rationalizes both the observed bi-exponential decay behavior and the non-linear Stern–Volmer response, thereby justifying the use of multi-site quenching models such as the simplified Lehrer model. The lifetime values in Pd and Pt porphyrins are about 980 μs and 71 μs (Table S4).[1,52] Values about 5 μs are found in Ru polypyridyl compounds and 480 μs with Ir cyclometalated compounds.[25] Thianthrene based compounds have much higher ms lifetimes.[11] The apparent quenching constant found for Mn-KF-part and Mn-TBAF-part are of 16 and 3 Pa^{-1} s^{-1} respectively, below about 20–70 Pa^{-1} s^{-1} for reference Pt or Ir compounds (Table S4).[52,56] We try to understand the difference in behavior between the two crystals Mn-KF-cryst and Mn-TBAF-cryst. One hypothesis lies in structural effects, such as porosity and coordination mode of the counter cation in the structure. In the Mn-KF-cryst, the pores have a maximum size of 4.1 Å without solvent and 2.1 Å with solvent (Mercury). The Mn-TBAF-cryst has a pore size of 3.1 Å with solvent. The Mn_4 clusters are more spaced since the counter cation TBA^+ is much bigger than K^+. Oxygen diffusion could therefore be easier in the Mn-TBAF-cryst than in the Mn-KF-cryst. This may be related to the sensitivity of the decay time (t_{long}) with oxygen content, from 1.87 to 0.73 ms, in Mn-TBAF-cryst. In both particles Mn-KF-part and Mn-TBAF-part, a high sensitivity is observed in short times, due to surface effects. The rapid component (t_{short}) accounts for 95% of the decline curve in the case of Mn-KF-part and only 48% of the decline in the case of Mn-TBA-part. Moreover, structural modifications are induced upon recrystallization, related to an increased porosity, accompanying the solvation of chains by DMF. Indeed, the Mn-KF-DMF-cryst (**3**) obtained after DMF recrystallization of the Mn-KF-cryst (**1**) has a coordination mode of potassium changing from 2 to 1. The crystal packing of the Mn-KF-DMF-cryst (**3**), and then in Mn-KF-part too, is more flexible than that of the Mn-KF-cryst (**1**). While crystallographic parameters cannot be directly translated into gas diffusion properties in the solid state, this structural change may indicate a more flexible molecular packing, which could facilitate oxygen accessibility at the local scale. Regardless of crystallographic packing considerations, the oxygen accessibility is directly evidenced by the oxygen-dependent lifetime component (t_{short}) and the significant quenchable fraction (86%) extracted from the Lehrer analysis. Nitrogen adsorption measurements indicate that Mn-KF-part have a much higher porosity compared to Mn-KF-cryst. This observation is completely coherent with the observed higher oxygen sensitivity of the particles Mn-KF-part. On the other hand, both Mn-TBAF-cryst and Mn-TBAF-part are found to be non-porous to nitrogen at 77 K while they are both sensitive to oxygen. This apparent contradiction could possibly be due to different flexibility depending on the temperature. It might be possible for the porosity of these compounds to be more flexible and blocked at 77 K, but not at room temperature.

Polymeric films containing Mn-KF-part or Mn-TBAF-part

Polyisobutylmethacrylate (PIBMA) and polystyrene (PS) polymers were used to prepare films on a glass substrate, containing these Mn-KF-part and Mn-TBAF-part.[57,58] Images obtained by optical microscopy and scanning electron microscopy (SEM) show that the particles appear as aggregates of a few microns in PIBMA films and a few tens of microns in PS films (Fig. S11). The Mn-KF-part are aggregated in the form of balls on the PS film. The high polarity of the particles explains why dispersion in these two non-polar polymers is not very favorable. In addition, classic de-wetting of PIBMA on glass is observed, due to the difference in surface energy between glass and PIBMA (70 mN m^{-1} and 33 mN m^{-1}). The thickness of these films is on the order of a few hundred nanometers as shown in SEM images after scraping the films with a razor blade (Fig. S11, 4th row). Despite the imperfect nature of these deposits, we wanted to verify whether these matrices disrupted the oxygen sensitivity of the particles they support. We observe optical properties that are preserved compared to those of unsupported particles (Fig. 6). The emission maximum is shifted to 608 and 628 nm for Mn-KF-part and Mn-TBAF-part in PIBMA. The Stern–Volmer representation of the intensities is shown in Fig. S12, with almost linear curves and K_{sv} values of 1.42 and 1.37 kPa^{-1} for Mn-K-part in PIBMA and PS films; lower sensitive but more linear answer is observed for Mn-TBAF-part in PIBMA and PS films with K_{sv} values of 0.37 and 0.44 kPa^{-1}. The evolution of the intensities reported according to the simplified Lehrer model (Fig. 6, 2nd row) shows that 95% of the sites of Mn-TBAF-part are sensitive to oxygen, with a K_{sv} factor of 0.67 kPa^{-1} in PIBMA and 0.52 kPa^{-1} in PS. The higher sensitivity of Mn-KF-part is confirmed in both PIBMA (K_{sv} = 1.86 kPa^{-1}) and PS (K_{sv} = 1.87 kPa^{-1}) with 96% of sites being sensitive (Table S3). The decay curves are shown in Fig. 7. The decay profile of unsupported particles is retained with a very rapid decrease in intensity in the case of films containing Mn-KF-part (Fig. 7), while the decrease is more gradual with films containing Mn-TBAF-part (Fig. 7). Analysis of the slopes of these curves (Fig. 7, 2nd row) also shows, in the short term, a very rapid initial component (of the order of 60 μs for Mn-KF-part and 110 μs for Mn-TBAF-part), which is sensitive to oxygen content. Furthermore, the decrease in this decay time is very noticeable for the lowest oxygen content (<12%) in the case of films containing Mn-KF-part. This decay is more gradual in films based on Mn-TBAF-part. The Lehrer representation of the evolution of the short component is shown (Fig. 7, 3rd row), with the curves $t_0/\Delta t$ as a function of $[O_2]^{-1}$. A linear response is obtained from which we can estimate the K_{sv} to 0.35 and

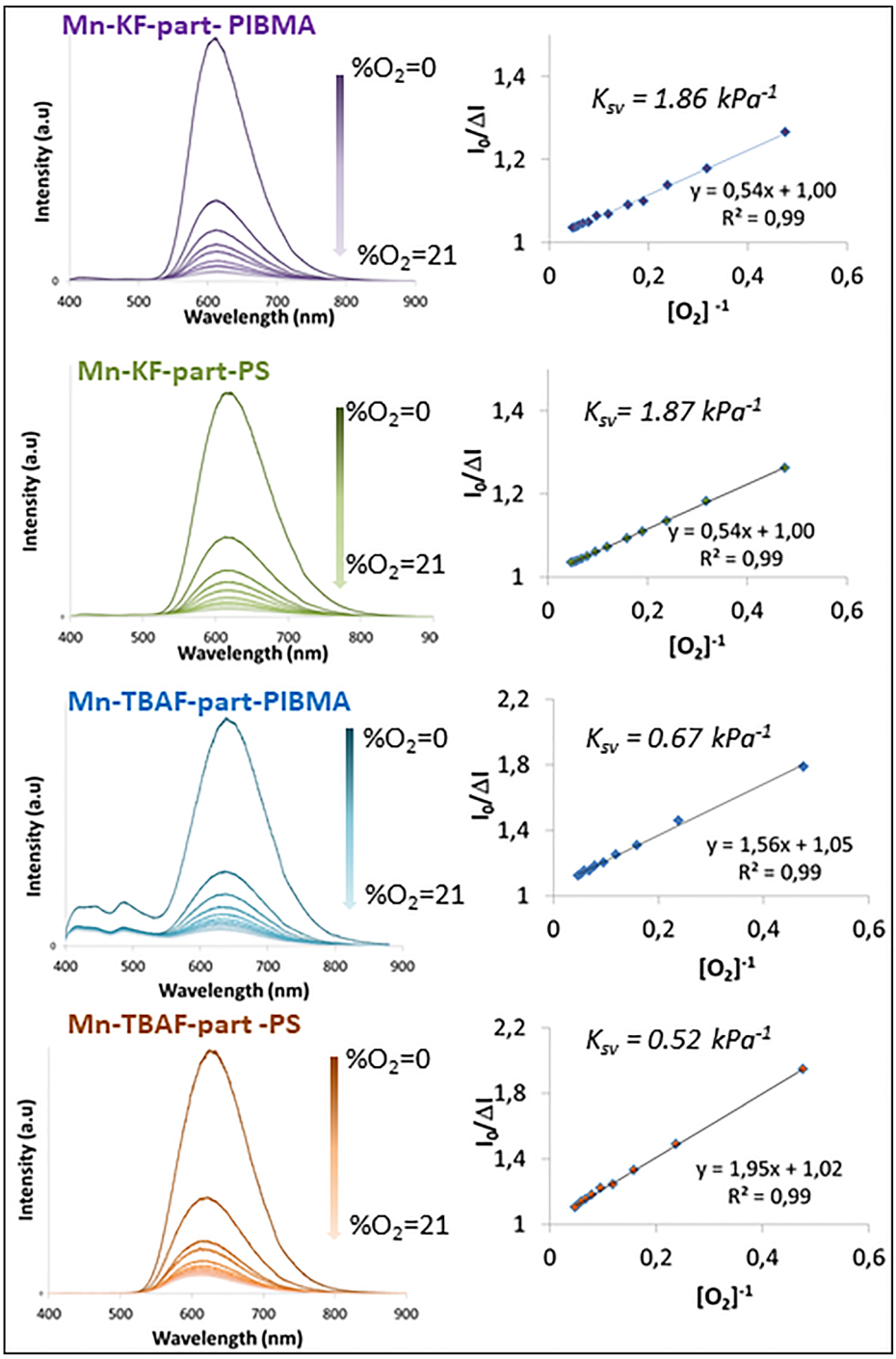

Fig. 6 Emission spectra of the Mn-TBAF-part and Mn-KFpart in PIBMA and PS matrixes at different O_2%. $I_0/\Delta I$ curves *versus* $[O_2]^{-1}$, of the Mn-TBAF-part and Mn-KF-part in PIBMA and PS matrixes at different O_2%.

0.76 kPa^{-1} in the Mn-KF-part-PIBMA and Mn-KF-part-PS films. In the case of Mn-TBAF-part, K_{sv} values of 0.35 and 0.55 kPa^{-1} have been measured in PIBMA and PS films, respectively.

The response time of Mn-TBAF-part and Mn-KF-part in PIBMA or PS films is illustrated by switching from nitrogen and air, which shows a rapid and stable response. The response in PIBMA films appears to be more stable than in PS films, probably due to better particle dispersion. The evolution of intensities between N_2 and air can be described using the two equations:

$$I(t) = I_{air} + \Delta I e^{\frac{-t}{\tau_{recovery}}}$$

$$I(t) = I_0 - \Delta I e^{\frac{-t}{\tau_{response}}}$$

where $\tau_{response}$ and $\tau_{recovery}$ are the response and recovery times

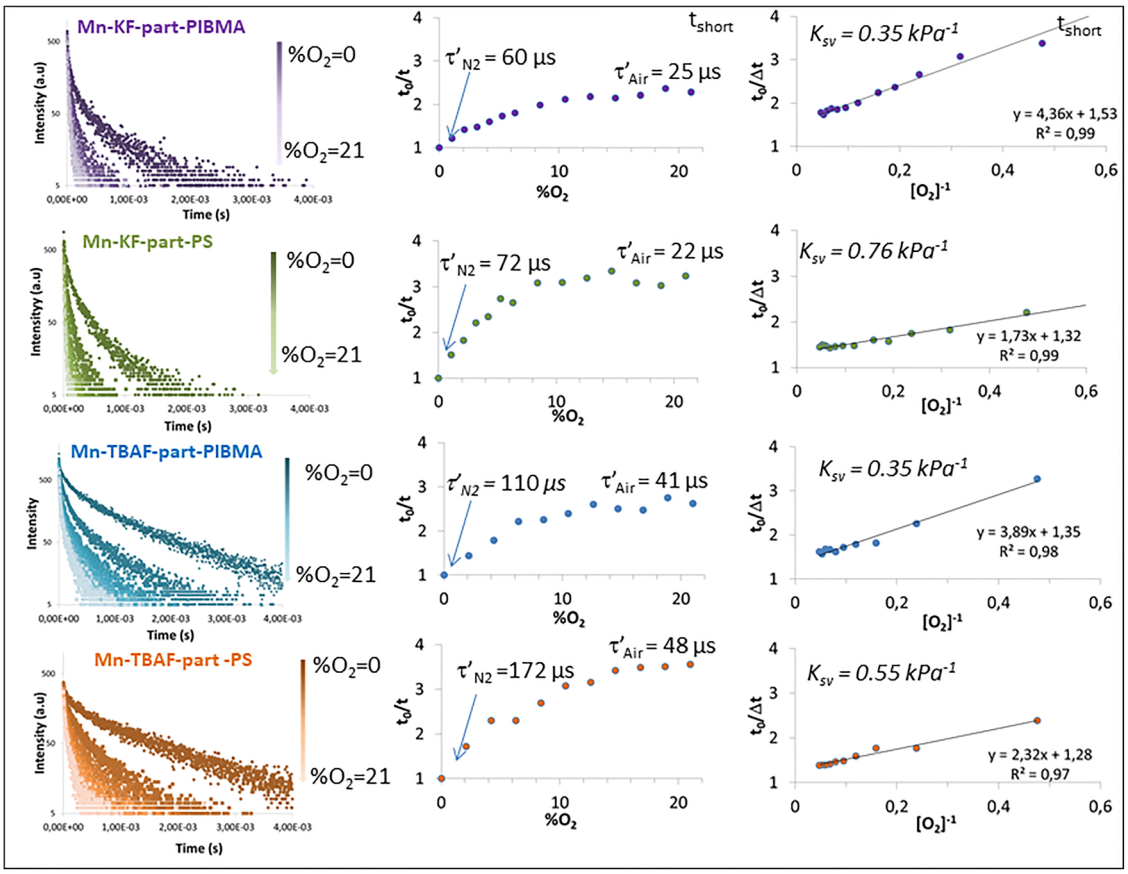

Fig. 7 Decay of the Mn-TBAF-part and Mn-KF-part in PIBMA and PS matrixes at different O_2%. Relative times of decay of the Mn-TBAF-part and Mn-KF-part in PIBMA and PS matrixes at different O_2% in the temporal zone (t_{short} < 150 µs). Relative times of decay $t_0/\Delta t$ of the Mn-TBAF-part and Mn-KF-part in PIBMA and PS matrixes at different O_2% in the temporal zone (t_{short} < 150 µs).

respectively. These response and recovery times are approximately 0.5 s and 7 s for the two Mn-KF-part containing films and 2 s and 9 s for the two Mn-TBAF-part containing films, as shown in Fig. 8. These response and recovery times (from N_2 to air) can be compared to some values obtained with the platinum(II) octaethylporphyrin Pt compound.[31,59] Response

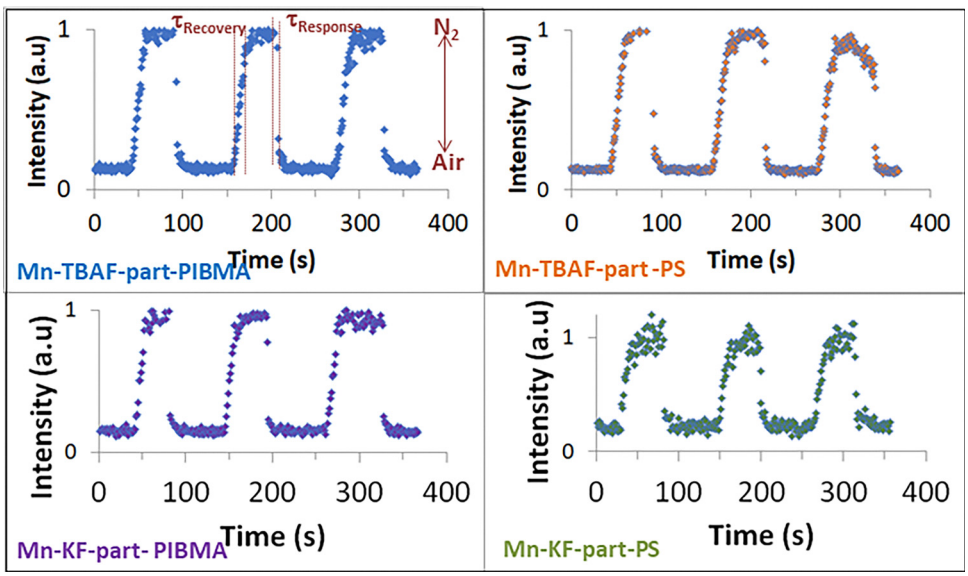

Fig. 8 Response time and intensity change for the Mn-TBAF-part and Mn-KF-part in PIBMA and PS matrixes on switching between nitrogen and air flux.

and recovery times, between O_2 and N_2, in this compound have been measured at 1.4 and 1.7 s, respectively in PDMS[59] or 0.3 s and 0.5 s, respectively in polymeric nanofibers.[31] Two videos provide a qualitative visualization of the dynamic response of the film in the case of TBAF particles in PIBMA. They show that the actual response and recovery times are shorter. The slow-motion film (4 times) in Movie S1, shows the Mn-TBAF-part in PIBMA sample with a flow of nitrogen. At the beginning of the film, the nitrogen is replaced by air. At 14 seconds (3.5 seconds in real time), oxygen arrives and the luminescence is rapidly quenched confirming a short response time. The second film (Movie S2) is a film of the Mn-TBAF-part in PIBMA sample under air, while a 2 L min^{-1} flow of N_2 from a 4 mm diameter tube is approached and moved around the sample. Bright areas appear instantly, indicating a very short recovery time (below 1 s). These two films clearly illustrate the fast reactivity of this material. Furthermore, the integration of a 5 × 5 pixel area of the film shows that the change in intensity between its maximum and minimum values occurs over a period of 300 ms (Fig. S13). It should be noted that the quoted value (∼300 ms) represents an estimate derived from a numerical analysis of a video, already used by other authors.[11] It should be regarded as an upper limit rather than a standardized response time. While the current polymer films are sufficient to demonstrate the oxygen-sensing performance of the complexes, further optimization of film morphology and dispersion will be required for practical device applications. The study of the influence of surface condition on reactivity should be undertaken by measuring grinding crystals. The samples tested can withstand exposure to the laser beam for several hours without degradation and do not change after several months. But long-term stability and photostability under continuous or repeated excitation were not investigated and remain important aspects for future work.

Conclusions

The Mn(II) sulfonylcalixarene complex based materials therefore have very interesting properties in terms of oxygen sensitivity. Their sensitivity is adapted for measuring high oxygen concentrations, as it prevents signal saturation and allows for linear and viable quantification over a wide range (generally between 1 and 21%). The influence of particle morphology and structure has an important impact on oxygen sensitivity and obtaining particles by dissolution in dimethylformamide followed by reprecipitation allows both smaller and more sensitive particles to be obtained. Oxygen diffusion is significantly favored in this structure. The study shows that the choice of counter-cation, between potassium and tetrabutylammonium, in these anionic complexes, also has an impact on oxygen sensitivity, related to structural effects. Lower sensitivity, but more consistent across the entire range of oxygen concentrations is observed with the tetrabutylammonium family. Very high sensitivity for the oxygen concentration range 0–12% is obtained with the potassium family. These Mn^{2+} sulfonylcalixarene complexes are ideally suited to detection applications in which conventional sensors are too sensitive and no longer linear. For example, they may be very suitable for monitoring oxygen concentrations in a laboratory, or industrial process, in the food industry, museum conservation, furnace control or aerodynamic studies where an oxygen sensor is used to measure partial pressure. Further work will focus on improving film homogeneity, substrate wetting, and large-area reproducibility to enable practical sensor implementations.

Author contributions

The manuscript was written by all the authors. All the authors have given approval to the final version of the manuscript.

Conflicts of interest

There are no conflicts to declare.

Data availability

The data supporting this article have been included as part of the supplementary information (SI). Supplementary information: X-ray data of the Mn-KF-cryst (**1**), Mn-TBAF-cryst (**2**) and Mn-KF-DMF-cryst (**3**) after recrystallization of (**1**) in DMF. Specific surface area (S), porous volume V_p, mesoporous volume V_{meso}, microporous volume V_{micro} (from t plot) and porous radius r_p from NLDFT, of the Mn-KF-cryst, Mn-KF-part, Mn-TBAF-cryst and Mn-TBAF-part. K_{sv}, from the Lehrer models calculated from intensity curves and from the short time component of the decay curves. I_0/I_{air} and t_0, and t_0/t_{air} from the decay curves (short times). Lifetime, K_{sv}, Stern–Volmer constant, k_q, quenching constant, t_0/t_{air} and I_0/I_{air} and response time of some reference oxygen sensors. Movie of the sample Mn-TBAF-part in PIBMA with a flow of nitrogen, at the beginning of the movie nitrogen is replaced by air; movie of the sample Mn-TBAF-part in PIBMA under air while a 2 L min^{-1} flow of N_2 getting out of a 4 mm diameter tubing is brought close to the sample and moved around. TEM images of Mn-KF-part; EDS analysis of the Mn-KF-cryst (a), Mn-TBAF-cryst (b), Mn-KF-part (c) and Mn-TBAF-part (d). Mass spectrometry of Mn-KF-part. FTIR spectra of the Mn-KF-cryst, Mn-KF-part (a) and Mn-TBAF-cryst, Mn-TBAF-part (b). Nitrogen adsorption isotherms (a), BJH pore size distribution (b) and NLDFT pore size distribution (c) of the Mn-KF-cryst and Mn-KF-part. Views of the packing of the Mn-KF complex (**1**) (a) and of the Mn-KF-DMF complex (**3**) (b) (F green, Mn purple, S yellow, O red, K blue, nitrogen blue, and carbon grey). Mercury contact surface visualization using probes of 1.2 Å in the Mn-KF-DMF complex (**3**). Relative photoluminescence intensity curves *versus* $\%O_2$ of the Mn-KF-cryst (a), Mn-TBAF-cryst (b), Mn-KF-part (c) and Mn-TBAF-part (d) at different $O_2\%$. Relative times of decay of the Mn-KF-cryst complex (a), Mn-KF-part (b), Mn-TBAF-cryst (c), and Mn-TBAF-part (d) at different $O_2\%$ in a temporal zones t_{long} between 0.6 and 2.6 ms. Relative $t_0/\Delta t$ curves *versus* $[O_2]^{-1}$ of the

Mn-KF-part (a) and Mn-TBAF-part (b) at different O_2%. Optical microscopy images (1st row) of Mn-TBAF-part, Mn-KF-part in PIBMA and PS matrixes. SEM images of Mn-TBAF-part, Mn-KF-part in PIBMA and PS matrixes (2nd row: global views; 3rd row: detailed views; 4th row: thickness views after scraping with a razor). Relative I_0/I curves *versus* %O_2 of Mn-TBAF-part and Mn-KF-part in PIBMA and PS matrixes at different O_2%. Integration of a square of 5 × 5 pixels from the movie of the sample Mn-TBAF-part in PIBMA with a flow of nitrogen, and at the beginning of the movie nitrogen is replaced by air. See DOI: https://doi.org/10.1039/d5tc04437e.

CCDC 2516881 contains the supplementary crystallographic data for this paper.[60]

Acknowledgements

The authors gratefully acknowledge the Ctμ platform of electronic microscopy (University Lyon 1).

References

1 X. Wang and O. S. Wolfbeis, Optical Methods for Sensing and Imaging Oxygen: Materials, Spectroscopies and Applications, *Chem. Soc. Rev.*, 2014, **43**(10), 3666–3761, DOI: 10.1039/C4CS00039K.

2 J. C.-M. Lee, J.-W. Li, K.-F. Cheng, J.-X. Chen, Y.-S. Ciou, J.-H. Wang, M.-C. Lu, Y.-F. Chen and C.-W. Chiu, Facile Fabrication and Analysis of Highly Sensitive PtTFPP/Carbon Black/Polystyrene Oxygen-Sensitive Composite Films for Optical Dissolved-Oxygen Sensor, *ACS Appl. Electron. Mater.*, 2024, **6**(3), 1617–1627, DOI: 10.1021/acsaelm.3c01508.

3 Y. Feng, J. Cheng, L. Zhou, X. Zhou and H. Xiang, Ratiometric Optical Oxygen Sensing: A Review in Respect of Material Design, *Analyst*, 2012, **137**(21), 4885, DOI: 10.1039/c2an35907c.

4 Y. Zhang, L. Zhou, Y. Du, H. Xu, X. Zhang, M. Wu, J. Xu, L.-Y. Chou and J. Chen, Biomineralization of Hemoglobin with ZIF-90 under Mild Conditions for Oxygen Sensing Application, *Inorg. Chem.*, 2025, **64**(31), 16168–16178, DOI: 10.1021/acs.inorgchem.5c02715.

5 X. Cai, H. Zhang, P. Wei, Q. Liu, D. Sheng, Z. Li, B. Zhang, G. Tang, W. Zhao, Z. Ye, Z. Xue, Y. Xie, Y. Dai, C. Wang, Y. Wang, X. Fu, L. Yin, H. Peng, H. Ding, G. Zhao and X. Sheng, A Wireless Optoelectronic Probe to Monitor Oxygenation in Deep Brain Tissue, *Nat. Photonics*, 2024, **18**(5), 492–500, DOI: 10.1038/s41566-023-01374-y.

6 T. Liang, C. Gu, J. Fang, D. Xu, Z. Wang, C. Chiappini and N. Hu, Cellular Metabolism Biosensing: From Extracellular Microenvironment to Intracellular Physiology Monitoring, *Biosens. Bioelectron.*, 2026, **295**, 118250, DOI: 10.1016/j.bios.2025.118250.

7 O. S. Wolfbeis, Luminescent Sensing and Imaging of Oxygen: Fierce Competition to the Clark Electrode, *BioEssays*, 2015, **37**(8), 921–928, DOI: 10.1002/bies.201500002.

8 J.-H. Lee, J.-H. Shin, K.-D. Seo, D.-S. Park and Y.-B. Shim, 3D Printed Oxygen Gas Sensor with a Pt-Nanoparticles Decorated N-Doped Carbon Catalyst and an Amine-Polymer Composited Ionic Liquid Gel Electrolyte, *Sens. Actuators, B*, 2025, **422**, 136657, DOI: 10.1016/j.snb.2024.136657.

9 Y. Wu, Y. Zou, J. Cheng, Y. Shu, B. Dai, K. Wang, D. Li, J. Han, S. Liu and J. Guo, Dynamic Oxygen Sensing Technology: Progress from Large-Scale Equipment to Portable Monitoring, *Biosens. Bioelectron.*, 2026, **294**, 118166, DOI: 10.1016/j.bios.2025.118166.

10 S. Nagl, C. Baleizão, S. M. Borisov, M. Schäferling, M. N. Berberan-Santos and O. S. Wolfbeis, Optical Sensing and Imaging of Trace Oxygen with Record Response, *Angew. Chem., Int. Ed.*, 2007, **46**(13), 2317–2319, DOI: 10.1002/anie.200603754.

11 Z. Yang, J. Qian, S. Zhao, Y. Lv, Z. Feng, S. Wang, H. He, S. Zhang, H. Liu and B. Yang, Highly Sensitive Thianthrene Covalent Trimer Room-Temperature Phosphorescent Materials for Low-Concentration Oxygen Detection, *Angew. Chem., Int. Ed.*, 2025, **64**(25), e202424669, DOI: 10.1002/anie.202424669.

12 E. Armagan, K. Wei, G. Fortunato, E. Amstad and R. M. Rossi, Reversible and Broad-Range Oxygen Sensing Based on Purely Organic Long-Lived Photoemitters, *ACS Appl. Polym. Mater.*, 2021, **3**(5), 2480–2488, DOI: 10.1021/acsapm.1c00064.

13 E. Mei, S. Vinogradov and R. M. Hochstrasser, Direct Observation of Triplet State Emission of Single Molecules: Single Molecule Phosphorescence Quenching of Metalloporphyrin and Organometallic Complexes by Molecular Oxygen and Their Quenching Rate Distributions, *J. Am. Chem. Soc.*, 2003, **125**(43), 13198–13204, DOI: 10.1021/ja030271k.

14 P. Ashokkumar, N. Adarsh and A. S. Klymchenko, Ratiometric Nanoparticle Probe Based on FRET-Amplified Phosphorescence for Oxygen Sensing with Minimal Phototoxicity, *Small*, 2020, **16**(32), 2002494, DOI: 10.1002/smll.202002494.

15 G. Schwendt and S. M. Borisov, Achieving Simultaneous Sensing of Oxygen and Temperature with Metalloporphyrins Featuring Efficient Thermally Activated Delayed Fluorescence and Phosphorescence, *Sens. Actuators, B*, 2023, **393**, 134236, DOI: 10.1016/j.snb.2023.134236.

16 A. Y. Lebedev, A. V. Cheprakov, S. Sakadžić, D. A. Boas, D. F. Wilson and S. A. Vinogradov, Dendritic Phosphorescent Probes for Oxygen Imaging in Biological Systems, *ACS Appl. Mater. Interfaces*, 2009, **1**(6), 1292–1304, DOI: 10.1021/am9001698.

17 A. C. Debruyne, I. A. Okkelman, N. Heymans, C. Pinheiro, A. Hendrix, M. Nobis, S. M. Borisov and R. I. Dmitriev, Live Microscopy of Multicellular Spheroids with the Multimodal Near-Infrared Nanoparticles Reveals Differences in Oxygenation Gradients, *ACS Nano*, 2024, **18**(19), 12168–12186, DOI: 10.1021/acsnano.3c12539.

18 J. Wu, Z. Huang, D. Kong and F. Huang, Polymer-Ceramic Pressure-Sensitive Paint with High Pressure Sensitivity and

Pressure-Sensitivity Constancy in Low-Pressure Environments, *Sens. Actuators, A*, 2024, **366**, 114900, DOI: 10.1016/j.sna.2023.114900.

19 J. Werner, M. Belz, K.-F. Klein, T. Sun and K. T. V. Grattan, Design and Comprehensive Characterization of Novel Fiber-Optic Sensor Systems Using Fast-Response Luminescence-Based O2 Probes, *Measurement*, 2022, **189**, 110670, DOI: 10.1016/j.measurement.2021.110670.

20 M. L. Bossi, M. E. Daraio and F. P. Aramendía, Luminescence Quenching of Ru(II) Complexes in Polydimethylsiloxane Sensors for Oxygen, *J. Photochem. Photobiol., A*, 1999, **120**(1), 15–21, DOI: 10.1016/S1010-6030(98)00418-3.

21 Y. Egami, A. Hasegawa, Y. Matsuda, T. Ikami and H. Nagai, Ruthenium-Based Fast-Responding Pressure-Sensitive Paint for Measuring Small Pressure Fluctuation in Low-Speed Flow Field, *Meas. Sci. Technol.*, 2021, **32**(2), 024003, DOI: 10.1088/1361-6501/abb916.

22 J. Feng, C. W. Baxter, I. V. Novosselov, G. Cao and D. Dabiri, Luminescent Pressure-Sensitive Paints with Embedded Ag@SiO_2 Nanoparticles, *ACS Appl. Nano Mater.*, 2025, **8**(1), 495–503, DOI: 10.1021/acsanm.4c05718.

23 M. Kasai, A. Suzuki, Y. Egami, T. Nonomura and K. Asai, A Platinum-Based Fast-Response Pressure-Sensitive Paint Containing Hydrophobic Titanium Dioxide, *Sens. Actuators, A*, 2023, **350**, 114140, DOI: 10.1016/j.sna.2022.114140.

24 Y. Mao, Z. Mei, J. Wen, G. Li, Y. Tian, B. Zhou and Y. Tian, Honeycomb Structured Porous Films from a Platinum Porphyrin-Grafted Poly(Styrene-Co-4-Vinylpyridine) Copolymer as an Optical Oxygen Sensor, *Sens. Actuators, B*, 2018, **257**, 944–953, DOI: 10.1016/j.snb.2017.11.042.

25 A. L. Medina-Castillo, J. F. Fernández-Sánchez, C. Klein, M. K. Nazeeruddin, A. Segura-Carretero, A. Fernández-Gutiérrez, M. Graetzel and U. E. Spichiger-Keller, Engineering of Efficient Phosphorescent Iridium Cationic Complex for Developing Oxygen-Sensitive Polymeric and Nanostructured Films, *Analyst*, 2007, **132**(9), 929, DOI: 10.1039/b702628e.

26 K. Mizukami, A. Katano, S. Shiozaki, T. Yoshihara, N. Goda and S. Tobita, In Vivo O2 Imaging in Hepatic Tissues by Phosphorescence Lifetime Imaging Microscopy Using Ir(III) Complexes as Intracellular Probes, *Sci. Rep.*, 2020, **10**(1), 21053, DOI: 10.1038/s41598-020-76878-6.

27 E. J. Nunn, D. Tsioumanis, G. F. S. Whitehead, T. B. Fisher, D. A. Roberts, M. K. Quinn and L. S. Natrajan, Exploring the Effect of Porphyrin Chemical Structure on the Performance of Polymer-Based Pressure-Sensitive Paints, *Sens. Actuators, B*, 2024, **409**, 135577, DOI: 10.1016/j.snb.2024.135577.

28 D. Yang, J. Ren, J. Li, Q. Wang, Q. Wang, Z. Xie and X. Qu, Construction of Bi-Layer Biluminophore Fast-Responding Pressure Sensitive Coating for Non-Contact Unsteady Aerodynamic Testing, *Polym. Test.*, 2019, **77**, 105922, DOI: 10.1016/j.polymertesting.2019.105922.

29 D. Yang, J. Li, J. Ren, Q. Wang, S. Zhou, Q. Wang, Z. Xie and X. Qu, Fast-Response Oxygen Sensitive Transparent Coating for Inner Pressure Ratiometric Optical Mapping, *J. Mater. Chem. C*, 2021, **9**(11), 3919–3927, DOI: 10.1039/D0TC06123A.

30 C.-S. Chu and Y.-L. Lo, High-Performance Fiber-Optic Oxygen Sensors Based on Fluorinated Xerogels Doped with Pt(II) Complexes, *Sens. Actuators, B*, 2007, **124**(2), 376–382, DOI: 10.1016/j.snb.2006.12.049.

31 P. Ludačka, V. Liška, J. Sýkora, P. Kubát and J. Mosinger, Luminescent Oxygen Sensor with Self-Sterilization Properties Based on Platinum(II)Octaethylporphyrin in Polymeric Nanofibers, *ACS Mater. Au*, 2025, **5**(2), 331–338, DOI: 10.1021/acsmaterialsau.4c00137.

32 F. Lin, X. Liu, M. Ye, J. Jin and X. Chen, Sensitive and Reversible Sensing of Oxygen Based on Transition Metals Doped Quasi-2D Layered Perovskites with 4T1 → 6A1 Luminescence, *Sens. Actuators, B*, 2025, **430**, 137382, DOI: 10.1016/j.snb.2025.137382.

33 C. Lecourt, Y. Suffren, E. Jeanneau, D. Luneau and C. Desroches, Mono-, Di-, and Tetranuclear Manganese(II) Complexes with *p* -Phenylsulfonylcalix[4]Arene Macrocycles as Ligand Antennas: Synthesis, Structures, and Emission Properties, *Cryst. Growth Des.*, 2022, **22**(4), 2279–2288, DOI: 10.1021/acs.cgd.1c01348.

34 M. Lamouchi, E. Jeanneau, A. Pillonnet, A. Brioude, M. Martini, O. Stéphan, F. Meganem, G. Novitchi, D. Luneau and C. Desroches, Tetranuclear Manganese(II) Complexes of Sulfonylcalix[4]Arene Macrocycles: Synthesis, Structure, Spectroscopic and Magnetic Properties, *Dalton Trans.*, 2012, **41**(9), 2707, DOI: 10.1039/c2dt11786j.

35 Y. Suffren, N. O'Toole, A. Hauser, E. Jeanneau, A. Brioude and C. Desroches, Discrete Polynuclear Manganese(II) Complexes with Thiacalixarene Ligands: Synthesis, Structures and Photophysical Properties, *Dalton Trans.*, 2015, **44**(17), 7991–8000, DOI: 10.1039/C5DT00827A.

36 I. O. Nasibullin, A. A. Sukhanov, A. G. Shmelev, I. A. Litvinov, V. K. Voronkova, E. I. Musina and A. A. Karasik, Macrocyclic Tetraphosphine Oxides as Scaffolds for Highly Luminescent and Thermally Stable 1D Manganese(II) Coordination Polymers, *Inorg. Chem. Commun.*, 2025, **182**, 115462, DOI: 10.1016/j.inoche.2025.115462.

37 P. Tao, S. Liu and W. Wong, Phosphorescent Manganese(II) Complexes and Their Emerging Applications, *Adv. Opt. Mater.*, 2020, **8**(20), 2000985, DOI: 10.1002/adom.202000985.

38 K. A. Vinogradova, A. S. Berezin, M. D. Taigina, V. A. Sannikova, I. R. Filippov, N. V. Pervukhina, D. Yu Naumov, D. S. Kolybalov and A. Yu Vorob'ev, White-Green Photoluminescence of Manganese(II) Complexes with Pyrazolo[1,5-a][1,10]Phenanthroline-3-Carbonitrile, *Inorg. Chim. Acta*, 2024, **569**, 122137, DOI: 10.1016/j.ica.2024.122137.

39 P. She, Z. Zheng, Y. Qin, F. Li, X. Zheng, D. Zhang, Z. Xie, L. Duan and W. Wong, Color Tunable Phosphorescent Neutral Manganese(II) Complexes Through Steric Hindrance Driven Bond Angle Distortion, *Adv. Opt. Mater.*, 2024, **12**(10), 2302132, DOI: 10.1002/adom.202302132.

40 L.-K. Gong, Q.-Q. Hu, F.-Q. Huang, Z.-Z. Zhang, N.-N. Shen, B. Hu, Y. Song, Z.-P. Wang, K.-Z. Du and X.-Y. Huang, Efficient Modulation of Photoluminescence by Hydrogen Bonding Interactions between Inorganic $[MnBr_4]^{2-}$ Anions and Organic Cations, *Chem. Commun.*, 2019, **55**(51), 7303–7306, DOI: 10.1039/C9CC03038G.

41 Y. Qin, P. She, X. Huang, W. Huang and Q. Zhao, Luminescent Manganese(II) Complexes: Synthesis, Properties and Optoelectronic Applications, *Coord. Chem. Rev.*, 2020, **416**, 213331, DOI: 10.1016/j.ccr.2020.213331.

42 I. V. Khariushin, V. Bulach, S. E. Solovieva, I. S. Antipin, A. S. Ovsyannikov and S. Ferlay, Thiacalix[4]Arene Macrocycles as Versatile Building Blocks for the Rational Design of High-Nuclearity Metallic Clusters, Metallamacrocycles, Porous Coordination Cages and Containers, *Coord. Chem. Rev.*, 2024, **513**, 215846, DOI: 10.1016/j.ccr.2024.215846.

43 C. Lecourt, G. Ledoux, Y. Suffren, E. Jeanneau, D. Luneau and C. Desroches, Multiphoton Excitation and Energy Transfer Pathways in Mn^{2+} –Sulfonyl Calixarene Complexes, *Dalton Trans.*, 2025, **54**(46), 17151–17161, DOI: 10.1039/D5DT02234G.

44 N. O'Toole, C. Lecourt, Y. Suffren, A. Hauser, L. Khrouz, E. Jeanneau, A. Brioude, D. Luneau and C. Desroches, Photogeneration of Manganese(III) from Luminescent Manganese(II) Complexes with Thiacalixarene Ligands: Synthesis, Structures and Photophysical Properties, *Eur. J. Inorg. Chem.*, 2019, (1), 73–78, DOI: 10.1002/ejic.201801104.

45 F. Hamada, Y. Higuchi, Y. Kondo, C. Kabuto and N. Iki, Supramolecular Assembly Based on π–π Stacking and π-Cation Interactions between Thiacalix[6]Arene and DMF, *Tetrahedron Lett.*, 2006, **47**(31), 5591–5593, DOI: 10.1016/j.tetlet.2006.05.055.

46 A. Kieliszek and M. Malinska, Conformations of *p-Tert* -Butylcalix[8]Arene in Solvated Crystal Structures, *Cryst. Growth Des.*, 2021, **21**(12), 6862–6871, DOI: 10.1021/acs.cgd.1c00773.

47 N. Hickey, V. Iuliano, C. Talotta, M. De Rosa, A. Soriente, C. Gaeta, P. Neri and S. Geremia, Solvent and Guest-Driven Supramolecular Organic Frameworks Based on a Calix[4]Arene-Tetrol: Channels vs Molecular Cavities, *Cryst. Growth Des.*, 2021, **21**(11), 6357–6363, DOI: 10.1021/acs.cgd.1c00828.

48 E. Zaorska, M. Stachowicz and M. Malinska, Preferential Crystallization of *Tert* -Butyl-Calix[6]Arene Chlorobenzene Solvate from a Solvent Mixture, *Cryst. Growth Des.*, 2023, **23**(5), 3455–3462, DOI: 10.1021/acs.cgd.3c00007.

49 O. I. Koifman, N. Zh Mamardashvili and O. V. Surov, Porous Molecular Crystals of Calix[4]Arenes, *Russ. Chem. Bull.*, 2017, **66**(2), 241–253, DOI: 10.1007/s11172-017-1724-9.

50 K. A. Udachin, G. D. Enright, P. O. Brown and J. A. Ripmeester, Pseudopolymorphism in the P-Tert-Butylcalix[4]Arene—n-Butylamine System: Directing the Structural Motifs, *Chem. Commun.*, 2002, 2162–2163, DOI: 10.1039/B204313K.

51 Y. Amao, I. Okura, H. Shinohara and H. Nishide, An Optical Sensing Material for Trace Analysis of Oxygen. Metalloporphyrin Dispersed in Poly(1-Trimethylsilyl-1-Propyne) Film, *Polym. J.*, 2002, **34**(6), 411–417, DOI: 10.1295/polymj.34.411.

52 S. M. Borisov, P. Lehner and I. Klimant, Novel Optical Trace Oxygen Sensors Based on Platinum(II) and Palladium(II) Complexes with 5,10,15,20-Meso-Tetrakis-(2,3,4,5,6-Pentafluorphenyl)-Porphyrin Covalently Immobilized on Silica-Gel Particles, *Anal. Chim. Acta*, 2011, **690**(1), 108–115, DOI: 10.1016/j.aca.2011.01.057.

53 R. W. Larsen and L. Wojtas, Photophysical Properties of [Ru(2,2′-Bipyridine) 3] 2+ Encapsulated within the Uio-66 Zirconium Based Metal Organic Framework, *J. Solid State Chem.*, 2017, **247**, 77–82, DOI: 10.1016/j.jssc.2016.12.028.

54 C. R. McKeithan, J. M. Mayers, L. Wojtas and R. W. Larsen, Photophysical Studies of Ru(II)Tris(2,2′-Bipyridine) Encapsulated within the ZnHKUST-1 Metal Organic Framework, *Inorg. Chim. Acta*, 2018, **483**, 1–5, DOI: 10.1016/j.ica.2018.07.047.

55 A. Chettri, J. Kruse, K. Kumar Jha, L. Dröge, I. Romanenko, C. Neumann, S. Kupfer, A. Turchanin, S. Rau, F. H. Schacher and B. Dietzek, A Molecular Photosensitizer in a Porous Block Copolymer Matrix-Implications for the Design of Photocatalytically Active Membranes, *Chem. – Eur. J.*, 2021, **27**(68), 17049–17058, DOI: 10.1002/chem.202102377.

56 T. Burger, M. V. Hernández, C. Carbonell, J. Rattenberger, H. Wiltsche, P. Falcaro, C. Slugovc and S. M. Borisov, Luminescent Porphyrinic Metal–Organic Frameworks for Oxygen Sensing: Correlation of Nanostructure and Sensitivity, *ACS Appl. Nano Mater.*, 2023, **6**(1), 248–260, DOI: 10.1021/acsanm.2c04301.

57 Y. Amao, T. Miyashita and I. Okura, Optical Oxygen Detection Based on Luminescence Change of Metalloporphyrins Immobilized in Poly(Isobutylmethacrylate-Co-Trifluoroethylmethacrylate) Film, *Anal. Chim. Acta*, 2000, **421**(2), 167–174, DOI: 10.1016/S0003-2670(00)01048-5.

58 M. Akram, M. H. Akhtar, M. Irfan and Y. Tian, Polymer Matrix: A Good Substrate Material for Oxygen Probes Used in Pressure Sensitive Paints, *Adv. Colloid Interface Sci.*, 2020, **283**, 102240, DOI: 10.1016/j.cis.2020.102240.

59 Z. Zhang, Y. Niu, H. Mu, J. Li, J. Wang and T. Liu, A Dual-Signal Ratiometric Optical Sensor Based on Natural Pine Wood and Platinum(II) Octaethylporphyrin with High Performance for Oxygen Detection, *Sensors*, 2025, **25**(13), 3967, DOI: 10.3390/s25133967.

60 CCDC 2516881: Experimental Crystal Structure Determination, 2026, DOI: 10.5517/ccdc.csd.cc2qh0qz.